Title

Efficient discontinuous finite difference meshes for 3-D Laplace-Fourier domain seismic wavefield modelling in acoustic media with embedded boundaries

Journal

Geophysical Journal International, 219(2)

ISSN

0956-540X

Authors

Alsalem, HJ
Petrov, P
Newman, G
et al.

Publication Date

2019-07-26

DOI

10.1093/gji/ggz361

Peer reviewed

Efficient discontinuous finite difference meshes for 3-D Laplace–Fourier domain seismic wavefield modelling in acoustic media with embedded boundaries

H.J. AlSalem,[1] P. Petrov,[2] G. Newman,[2] E. Um[2] and J. Rector[1]

[1]Department of Civil Engineering, University of California-Berkeley, 2594 Hearst Ave, Berkeley, CA 94709, USA. E-mail: geohussain@berkeley.edu
[2]Lawrence Berkeley National Laboratory, 67 Centennial Dr, Berkeley, CA 94705, USA

SUMMARY

Simulation of acoustic wave propagation in the Laplace–Fourier (LF) domain, with a spatially uniform mesh, can be computationally demanding especially in areas with large velocity contrasts. To improve efficiency and convergence, we use 3-D second- and fourth-order velocity-pressure finite difference (FD) discontinuous meshes (DM). Our DM algorithm can use any spatial discretization ratio between meshes. We evaluate direct and iterative parallel solvers for computational speed, memory requirements and convergence. Benchmarks in realistic 3-D models and topographies show more efficient and stable results for DM with direct solvers than uniform mesh results with iterative solvers.

Key words: Seismic; Finite-difference; Acoustic waves; High performance computing; Frequency domain.

1 INTRODUCTION

Finite-difference (FD) methods that solve the acoustic wave equation over a discrete set of gridpoints have the advantage of being able to handle realistic geological structures of arbitrary complexity (Graves 1996). However, their computational cost grows with the number of required grid nodes (Operto *et al*. 2007; Fichtner 2011). One of the important reasons is the high contrast of seismic-wave velocities found in real earth structures, especially in arid environments where the near-surface velocity is low. Other reasons include requiring more gridpoints for 3-D models (vs. 2-D), and applying a high-frequency point source. Most algorithms of wave propagation either ignore the relatively thin low-velocity regions or include them using a uniform grid size that is determined by the lowest velocity, which has the shortest wavelength (Nie *et al*. 2017). The first simulation produces inaccurate results which causes the simulated data to misrepresent the true data. The second simulation results in oversampling the deeper regions with higher velocity inevitably leading to a considerable increase of computational time and memory. For these reasons, it is preferable to use different discretizations in shallow and deep regions.

There are several other numerical solution methods naturally suited for modelling seismic fields over complex surfaces. For example, finite element (FE) methods solve a system of equations derived from a weak form of the

wave equation. Using unstructured grids (e.g. tetrahedral meshes), FE methods can accurately and economically discretize arbitrary complex topography and horizons (Bao *et al*. 1998). Spectral element (SE) methods (Komatitsch & Tromp 1999) are similar to the p version of FE methods (Jin 2015) and can also discretize a computational domain into unstructured meshes adapted to irregular surfaces.

However, their advantage over FD methods come with extra complications. For example, it is not straightforward to develop an effective regularization matrix for tetrahedral meshes (Zhang 2017). Generation, visualization and analysis of tetrahedral meshes are also cumbersome and difficult especially when fine scale elements for complex irregular surface and faults are mixed with large scale elements for regional geology (Casarotti *et al*. 2008). Fast and accurate generation and display of large multiscale tetrahedral meshes is currently an active research area in computational mathematics and engineering. In contrast, the use of the structured FD grids allows us to easily and rapidly construct, visualize and analyse earth models. More importantly, from a practical point of view, most geoscience modelling tools are built on rectangular meshes. Thus, the use of rectangular meshes in seismic modelling allows us to import and export velocity models to flow and reservoir simulators.

Several authors have developed FD methods with variable grid spacing. Moczo (1989) and Pitarka (1999) developed FD methods with grid spacing changing gradually over a distance separating a fine and coarse mesh, which are less efficient and less flexible to apply as compared to discontinuous mesh (DM) methods. To accurately and efficiently model realistic geological structures, other varieties of DM methods have been proposed (e.g. Aoi & Fujiwara 1999; Tessmer 2000; Hayashi *et al*. 2001; Wang *et al*. 2001; Kristek *et al*. 2010; Zhang *et al*. 2012). The time-domain FD DM implementations suffer inherently from stability problems after a large number of time steps (Nie *et al*. 2017).

In this paper, we introduce a DM into second- and fourth-order LF domain velocity-pressure staggered FD scheme with topography to simulate acoustic wave propagation. The uniform grid acoustic implementation from Petrov & Newman (2012) and AlSalem *et al*. (2018) is now developed to be highly scalable using PETSc numerical libraries (Balay *et al*. 2018). Simulations are being pushed to higher frequencies with realistic 3-D heterogeneous velocity models to meet the requirements of gas and oil exploration in arid environments. Here, we introduce an interface between fine and coarse meshes and benchmark the method for accuracy, convergence and efficiency. We evaluate direct and iterative parallel solvers that are included in PETSc for computational speed, memory requirements and convergence. These validation tests include a simple homogeneous model in a sloping free surface, a low contrast layered velocity model underlying a hill free surface and a high contrast layered velocity model underlying realistic topography provided by Saudi Aramco.

2 DISCONTINUOUS MESH IMPLEMENTATION

2.1 Theory

Frequency-domain modelling of wave propagation inside the earth has been studied extensively (see Lysmer & Drake 1972; Marfurt 1984; Pratt & Worthington 1990; Zahradník & Urban 1984; Jo *et al*. 1996; Štekl & Pratt 1998; Hustedt *et al*. 2004; Operto *et al*. 2007). Most of the methods that have been developed for wave modelling in the frequency domain are based on solving the acoustic wave equation by the FD method: on a uniform grid, the FD methods provide an excellent compromise between accuracy and computational efficiency.

We consider the first-order hyperbolic system in a velocity–pressure formulation in the LF domain, which can be derived from Petrov & Newman (2012). Let the 3-D isotropic acoustic medium with density ρ and incompressibility κ occupy the region Ω. The equations of motion inside Ω are given by:

$$\begin{aligned} s\rho v_x &= \partial_x P, \\ s\rho v_y &= \partial_y P, \\ s\rho v_z &= \partial_z P, \\ sP &= \kappa \left[\partial_x v_x + \partial_y v_y + \partial_z v_z\right] + sm, \end{aligned} \tag{1}$$

where s is the complex number given by σ + iω, σ is the Laplace damping factor, ω is the angular frequency and $i = \sqrt{-1}$. The velocities v_x, v_y and v_z are the velocity wavefield components, P is the acoustic pressure, m is seismic moment density tensor and the symbols ∂_x, ∂_y and ∂_z denote the partial differential operators $\frac{\partial}{\partial x}$, $\frac{\partial}{\partial y}$ and $\frac{\partial}{\partial z}$, respectively. The LF equations of motion (eq. 1) are obtained by transforming the time-domain system of equations (Virieux 1986) using the following LF transform:

$$g(s) = \int_0^\infty g(t) e^{-st} \mathrm{d}t, \tag{2}$$

where $g(t)$ includes the functions $v_x(t)$, $v_y(t)$, $v_z(t)$ and $P(t)$.

For the numerical solution of eq. (1), we use FD schemes with seven point-stencils for second-order and 19 point-stencils for fourth-order approximation (Operto *et al*. 2007). This system of equations must be augmented with boundary conditions. In the case of infinite media, the non-reflecting condition for wavefield components is applied at the boundaries of region Ω.

We used the perfectly matched layer (PML) boundary conditions (Hastings *et al*. 1996; Kim & Pasciak 2010). At the free surface boundary, one needs to incorporate the following boundary condition:

$$P = 0, \tag{3}$$

which is realized for any simple or complicated topographic structure using our embedded boundary method (Li *et al*. 2010; AlSalem *et al*. 2018).

In typical seismic models, the velocity and density tend to increase with depth. Hence, simulation of seismic wave propagation using a spatially uniform mesh can be computationally very demanding due to the overdiscretization of the high-velocity material. Thus, small grid sizes can be used at the top and larger grid sizes can be used at deeper regions of the model. This issue can be partly addressed by varying grid sizes (Δz) with depth. However, lateral grid sizes (Δx and Δy) are still constrained by the global minimum velocity (Pasalic & McGarry 2010). One approach is to discontinuously vary Δx, Δy and Δz grid sizes along the z direction to take advantage of variations in velocity. Fig. 1 shows the layout of the three velocity components and acoustic pressure, indicating that the most basic way to implement a DM is to use a ratio of spatial discretization H/h between the coarse (H) and the fine (h) grids. In this example, we consider the case of $H/h = 3$ to demonstrate the advantage of the DM method. Updating v_x in a high-velocity material using the uniform second-order FD method requires pressure values at $\pm(1/2)h$, while the DM method skips the nearest pressure values and uses $\pm(3/2)h$ instead.

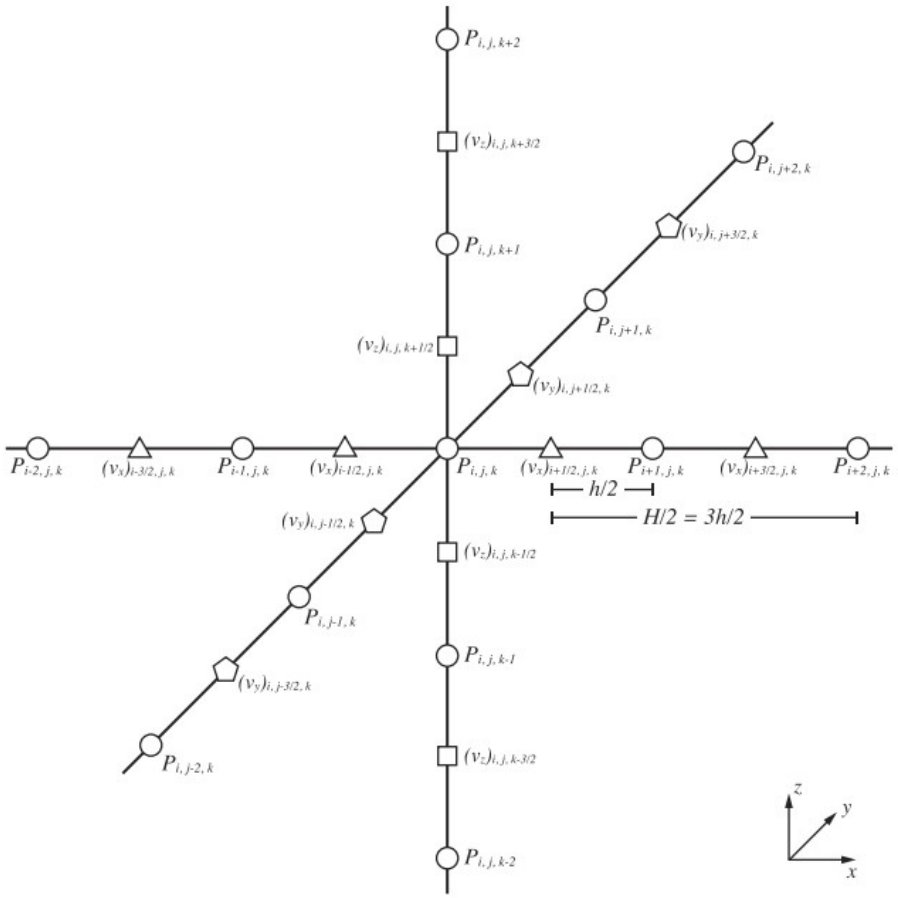

Figure 1. Layout of pressure and velocity components for staggered-grid acoustic wave propagation FD method. Updating $(v_x)_{i+1/2,j,k}$ requires $P_{i,j,k}$, and $P_{i+1,j,k}$ for second-order FD and $P_{i-1,j,k}$, $P_{i,j,k}$, $P_{i+1,j,k}$, $P_{i+2,j,k}$ for fourth-order FD approximation. A second-order DM method with a ratio of grid spacing (H/h) of three skips the nearest pressure components at $P_{i,j,k}$, and $P_{i+1,j,k}$ and uses values at $P_{i-1,j,k}$, and $P_{i+2,j,k}$ to update $(v_x)_{i+1/2,j,k}$ instead.

Since the velocity components are partial derivatives of acoustic pressure (eq. 1), we focus on only illustrating the acoustic pressure values in the DM FD approximation. Our approach divides the model into a number of regions, separated by horizontal planes (Fig. 2). Within each region, Δx, Δy and Δz are uniform and equal; however, they vary from one region to another. In this way, discretization becomes a discontinuous function of depth.

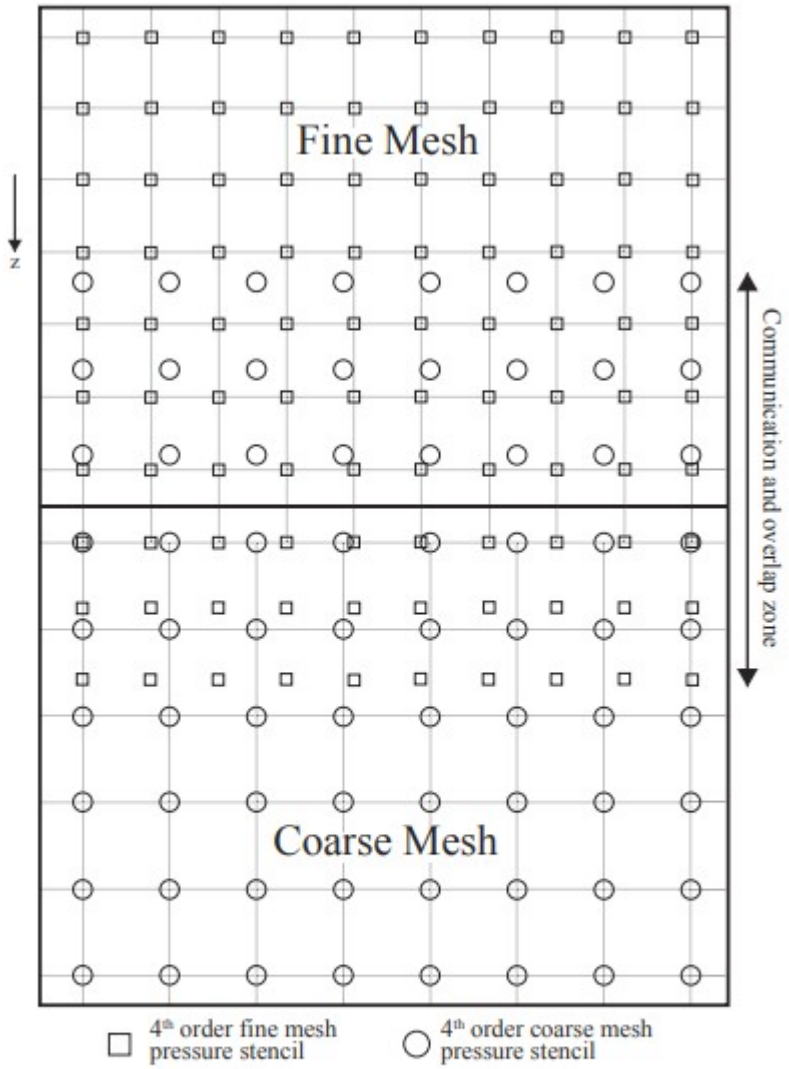

Figure 2. Communication between a fine and coarse mesh in 2-D for fourth-order FD scheme. Overlapped stencils for each region in 2-D are found using simple bilinear interpolation for three layers of stencils. The interface between the differently spaced meshes is shown as a bold horizontal line.

2.2 Communication across region interfaces

In each discontinuous region, the wave propagation FD discretization can be performed as for the uniform mesh. However, we clearly need to have some communication across the regions' interfaces (Fig. 2). To demonstrate the communication, we consider a fourth-order FD example with two 1-D regions as illustrated in Fig. 3. The spacing ratio between the coarse and fine regions is $H/h = 1.5$. The open nodes in the figure are approximated using fourth-order FD while the filled nodes are approximated using interpolation and downsampling to update the missing fine grid and coarse grid nodes, respectively. To realize these approximations in one matrix, we provide the following steps:

i. Generate fine- and coarse-mesh 1-D fourth-order FD matrices for each region with grid sizes h and H, respectively:

$$A_{\mathrm{f}} = \begin{bmatrix} A_{f_{11}} & A_{f_{12}} \\ A_{f_{21}} & A_{f_{22}} \end{bmatrix}, \quad A_{\mathrm{c}} = \begin{bmatrix} A_{c_{11}} & A_{c_{12}} \\ A_{c_{21}} & A_{c_{22}} \end{bmatrix}. \tag{4}$$

Here, A_{f} and A_{c} are the fourth-order FD square matrices for the fine and coarse regions, respectively. A_{f} includes n_{f} fine grid nodes (rows) in the fine region plus three fine grid nodes (rows) in the coarse region. Similarly, A_{c} includes n_{c} coarse grid nodes in the coarse region plus three coarse grid nodes in the fine region as shown in Fig. 3. Using this information, we split A_{f} to four submatrices where the size of $A_{f_{11}}$ is ($n_{\mathrm{f}} \times n_{\mathrm{f}}$), $A_{f_{12}}$ is ($n_{\mathrm{f}} \times 3$), $A_{f_{21}}$ is ($3 \times n_{\mathrm{f}}$), and $A_{f_{22}}$ is (3×3). Inversely, we split A_{c} into four submatrices where the size of $A_{c_{11}}$ is (3×3), $A_{c_{12}}$ is ($3 \times n_{\mathrm{c}}$), $A_{c_{21}}$ is ($n_{\mathrm{c}} \times 3$), and $A_{c_{22}}$ is ($n_{\mathrm{c}} \times n_{\mathrm{c}}$).

ii. Remove rows containing non-regional grid nodes $(A_{f_{21}}, A_{f_{22}}, A_{c_{11}} \text{ and } A_{c_{12}})$ in the square matrices (A_{f} and A_{c}) and keep the regional grid nodes $(A_{f_{11}} \text{ and } A_{c_{22}})$ and their communication stencils $(A_{f_{12}} \text{ and } A_{c_{21}})$. We end up with the following rectangular matrices:

$$A'_f = \begin{bmatrix} A_{f_{11}} & A_{f_{12}} \end{bmatrix}, \quad A'_c = \begin{bmatrix} A_{c_{21}} & A_{c_{22}} \end{bmatrix}. \tag{5}$$

iii. Generate the coarse to fine grid linear interpolation (trilinear interpolation in 3-D) matrix depending on the positions of the interpolated fine grid nodes (filled squares) in Fig. 3:

$$A_{fc} = \begin{bmatrix} 1 & 0 & 0 \\ \frac{1}{3} & \frac{2}{3} & 0 \\ 0 & \frac{2}{3} & \frac{1}{3} \end{bmatrix}.$$

(6)

iv. Generate the fine to coarse grid linear downsampling (trilinear downsampling in 3-D) matrix depending on the positions of the downsampled coarse grid nodes (filled circles) in Fig. 3:

$$A_{cf} = \begin{bmatrix} \frac{1}{2} & \frac{1}{2} & 0 & 0 & 0 \\ 0 & 0 & 1 & 0 & 0 \\ 0 & 0 & 0 & \frac{1}{2} & \frac{1}{2} \end{bmatrix}.$$

(7)

v. Merge the matrices together to get the fourth-order DM FD square matrix for two regions:

$$A_{DM} = \begin{bmatrix} A_{f_{11}} & A_{f_{12}} \cdot A_{fc} \\ A_{c_{21}} \cdot A_{cf} & A_{c_{22}} \end{bmatrix}.$$

(8)

We call $A_{f_{11}}$ and $A_{c_{22}}$ the forward modelling operators and $A_{f_{12}} \cdot A_{fc}$ and $A_{c_{21}} \cdot A_{cf}$ the interpolation and downsampling operators, respectively. We pad the right side of the interpolation operator and the left side of the downsampling operator with zeros to ensure the matrix is square. We can rewrite the linearlized problem for two regions as:

$$\begin{bmatrix} A_{f_{11}} & A_{f_{12}} \cdot A_{fc} \\ A_{c_{21}} \cdot A_{cf} & A_{c_{22}} \end{bmatrix} \begin{bmatrix} P_f \\ P_c \end{bmatrix} = \begin{bmatrix} F_f \\ F_c \end{bmatrix},$$

(9)

where the size of each of P_f and F_f is n_f, and the size of each of P_c and F_c is n_c.

We observe from eq. (9) that the communication stencils $A_{f_{12}}$ and $A_{c_{21}}$ are linked to the differently spaced grid nodes using the interpolation A_{fc} and downsampling A_{cf} matrices, respectively.

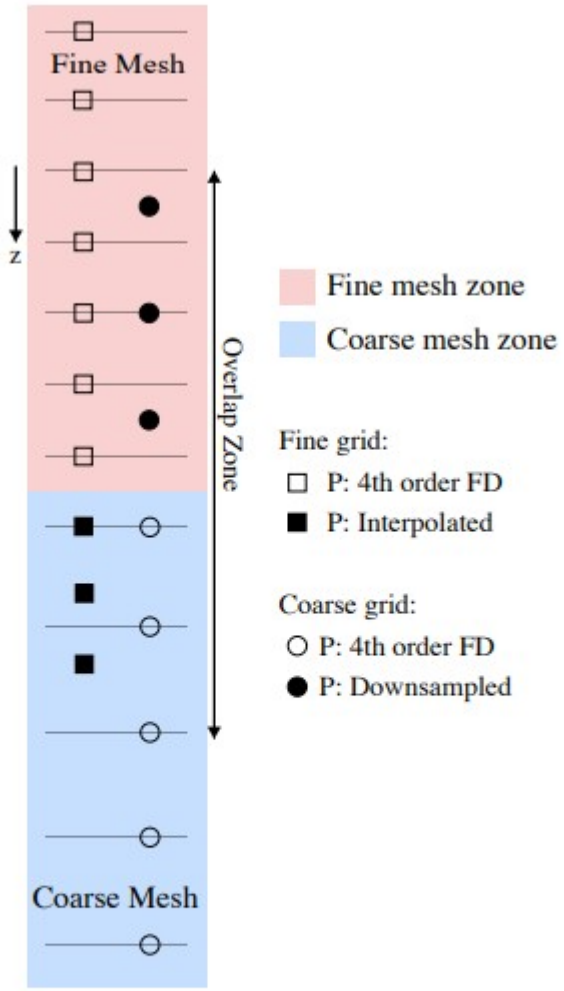

Figure 3. Distribution of fourth-order FD acoustic pressure nodes on the z-axis in the overlap zone between the fine and coarse meshes. Open symbols represent nodes that are fourth-order accurate. The filled squares represent nodes that are interpolated from the coarse grid nodes and filled circles represent nodes that are downsampled from the fine grid nodes.

For the 3-D case, this is done by simple trilinear interpolation and downsampling across the relevant acoustic pressure values from one region to another for any H/h ratio. Hence, using FD, the acoustic wave propagation in LF domain can be approximated by:

$$\begin{bmatrix} 1 & A_{1,2} & 0 & \cdots & 0 \\ A_{2,1} & A_2 & A_{2,3} & \ddots & \vdots \\ 0 & \ddots & \ddots & \ddots & 0 \\ \vdots & \ddots & A_{n-1,n-2} & A_{n-1} & A_{n-1,n} \\ 0 & \cdots & 0 & A_{n,n-1} & A_n \end{bmatrix} \begin{bmatrix} 1 \\ \vdots \\ P_n \end{bmatrix} = \begin{bmatrix} 1 \\ \vdots \\ F_n \end{bmatrix}, \tag{10}$$

where A_i is the forward modelling operator for region i, $A_{i,j}$ is the interpolation or downsampling operator from region j to region i, and P_i and F_i are the acoustic pressure and source function for region i, respectively.

The proposed DM FD scheme is a flexible technique that brings significant savings in computational effort and memory requirements. However, certain constraints must be observed. The most important is the number of communication layers across the region interfaces (Fig. 2). To ensure minimum reflection from the interface, the communication will occur over two and six layers (planes for 3-D case) in z-direction for second- and fourth-order FD schemes, respectively. We call the communication layers overlapping planes because it is where differently spaced gridpoints overlap in 3-D.

3 ACCURACY OF DM

To verify the accuracy of our DM with embedded boundary FD method, we present three scenarios: a homogeneous velocity model with a sloping free surface, a layered velocity model with a hill free surface and a layered velocity model with realistic topography. For all the tests, we use a point-source and receivers slightly below the surface. The accuracy of our first test is compared with the analytical solution while the following tests are compared with the uniform fine mesh solution that has been thoroughly verified with respect to analytical solutions in AlSalem *et al*. (2018). For these comparisons, relative error is calculated by:

$$e_{DM}(\mathbf{r}_\Omega, s) = \frac{\big|\ |P_{sim}(\mathbf{r}_\Omega, s)| - |P_R(\mathbf{r}_\Omega, s)|\ \big|}{|P_R(\mathbf{r}_\Omega, s)|} \times 100, \tag{11}$$

where $\mathbf{r}_\Omega \in$ region Ω, s is the Laplace–Fourier complex frequency, P_{sim} is the simulation result and P_{R} is the reference solution.

3.1 Homogeneous model with a sloping free surface

The first experiment is performed on a homogeneous velocity model, with a velocity of 5000 m s^{-1} and a density of 2000 kg m^{-3} (Fig. 4). The excitation is applied 20 m below and normal to the 10° sloping free surface. Grid spacing discontinuously increases with depth in such a way as to ensure a minimum of eight points per shortest wavelenghth. A Ricker wavelet with a frequency of 20 Hz and damping $1\frac{1}{s}$ is used as the source waveform. Observation points are placed 5 m below and normal to the sloping free surface.

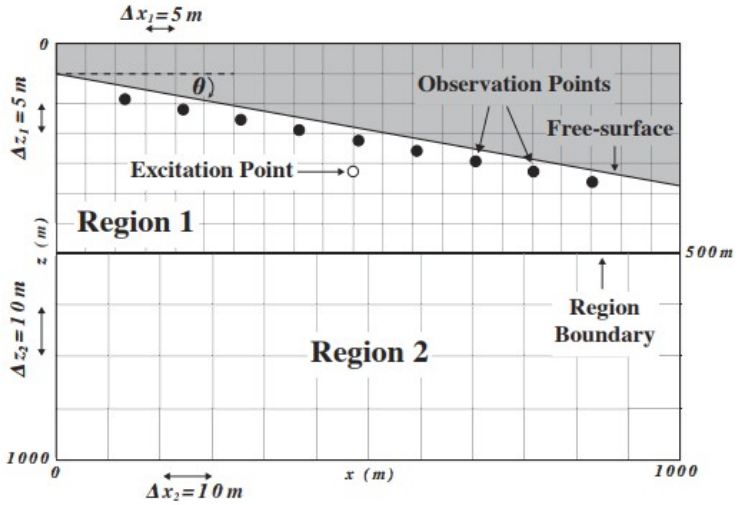

Figure 4. Mesh consisting of a sloping free surface and two discontinuous regions. The near-surface observation points are used for calculation of error caused by the embedded boundary and DM methods for a homogeneous model.

In the experiment, the DM with embedded boundary method is applied on a second-order FD scheme to calculate the pressure response at observation points. Here, we use two overlapping planes for communication since the FD scheme is second-order. In Fig. 5, we compare the absolute acoustic pressure values obtained by the analytical solution and DM with embedded boundary. Overall, the average error for the DM method is less than 5 per cent (Fig. 6).

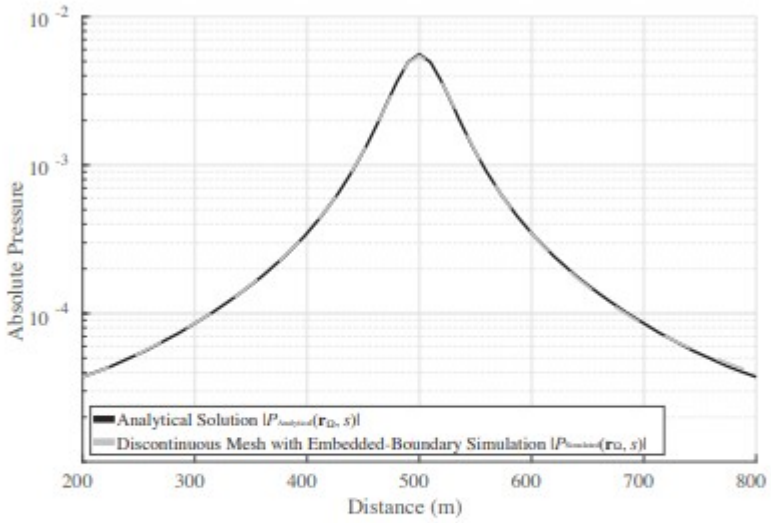

Figure 5. Absolute pressure for second-order DM FD with embedded boundary at the observation points in Fig. 4. The plot demonstrates the solution for a frequency of 20 Hz with damping $1\frac{1}{s}$ relative to the analytical solution.

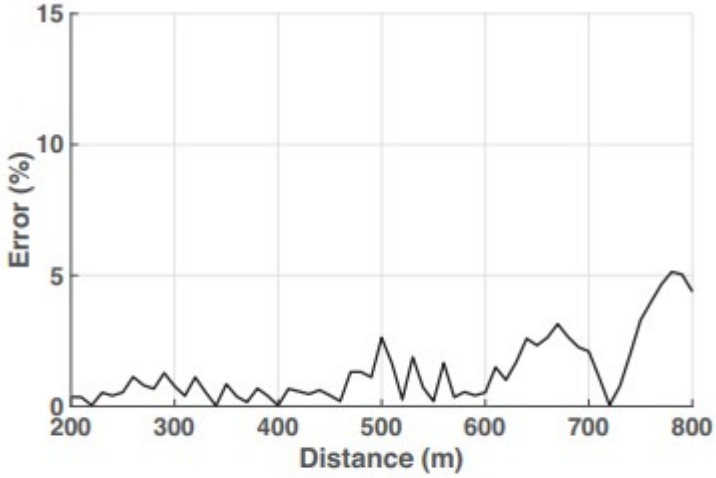

Figure 6. Error for second-order DM FD scheme with embedded boundary relative to the analytical solution.

3.2 Layered model with a hill as free surface

Here, we apply our DM scheme to a layered velocity model under a hill as the free surface. The hill topography and two depth slices, illustrating the layered velocity model with source and receiver locations are shown in Fig. 7. The density is 2000 kg m^3 for all the layers. The uniform simulations have a constant grid size of 5 m. For the DM FD simulations, we place the DM interface at a depth of 750 m, above which the grid size is 5 m, and below which we use 10 m. The overlap zone contains 2 and 6 overlapping planes

for the second- and fourth-order DM FD simulations, respectively. The point source is located at (100, 500, 540) m, 40 m below the free surface (Fig. 7b). We apply a Ricker-wavelet source with a central frequency of 20 Hz. For both the fine- and coarse-grid regions, we sample the minimum spatial wavelength by at least eight nodes.

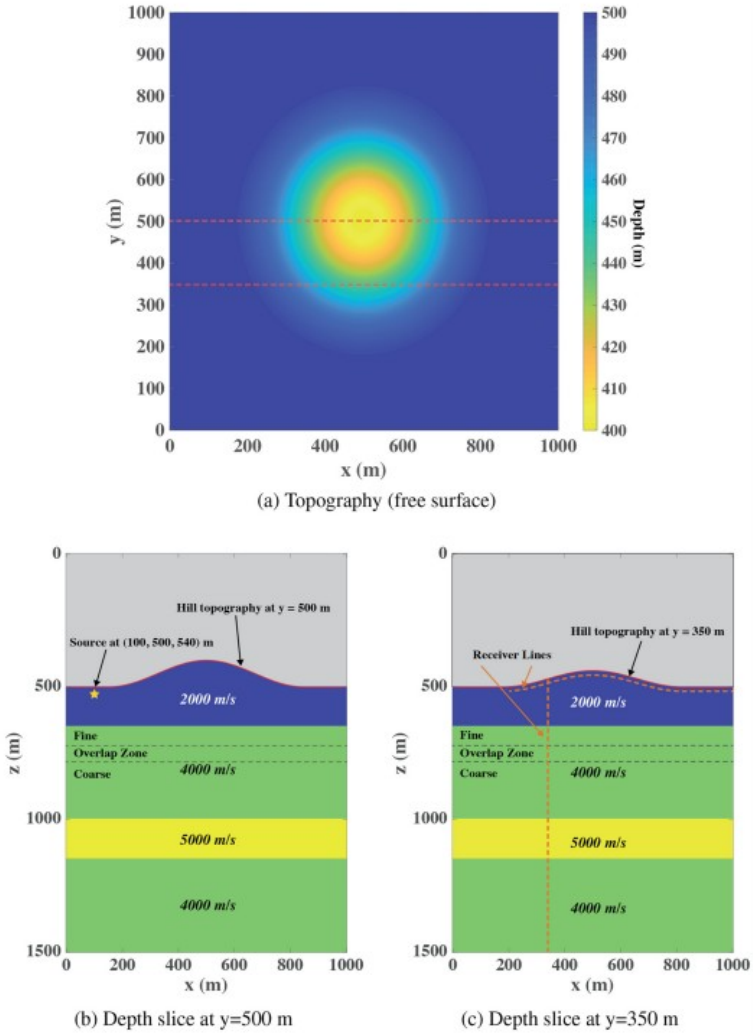

Figure 7. (a) Topography of the hill free surface with two *red* lines for cross-sections (b) at $y = 500$ m and (c) at $y = 350$ m. Cross-section (b) shows the source location and cross-section (c) shows the receiver lines.

We compare acoustic pressure solutions between the uniform and DM spatial discretizations at two receiver lines: one is aligned along and 10 m below the free surface and the other is aligned along the z direction and located at $x = 350$ m (see Fig. 7c). The uniform and DM solutions are nearly identical to the naked eye in both the real and imaginary parts for second- and fourth-order FD solutions (see Figs 8 and 9), with an average error of less than 5 per cent as shown in Fig. 10.

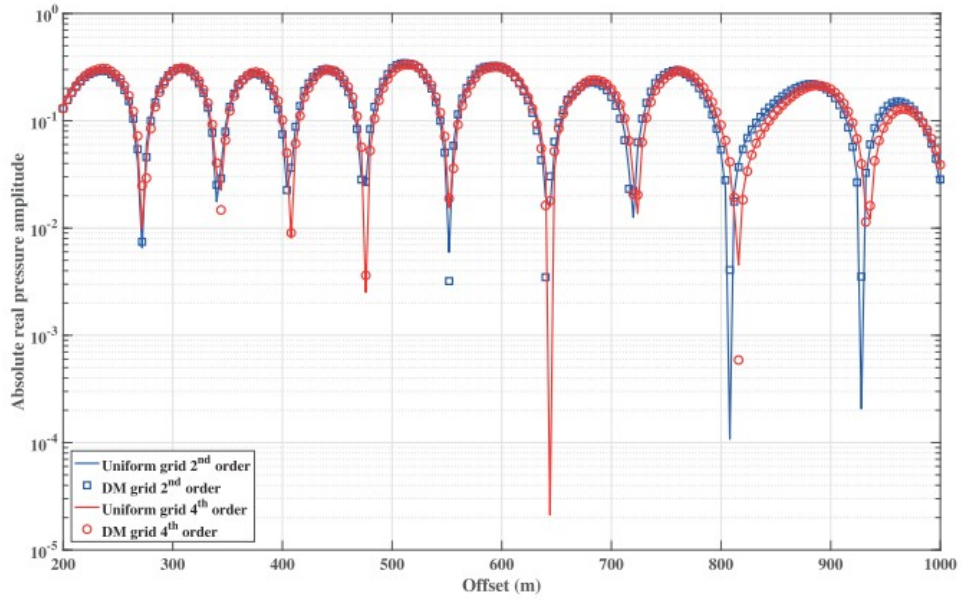

(a) Absolute real part

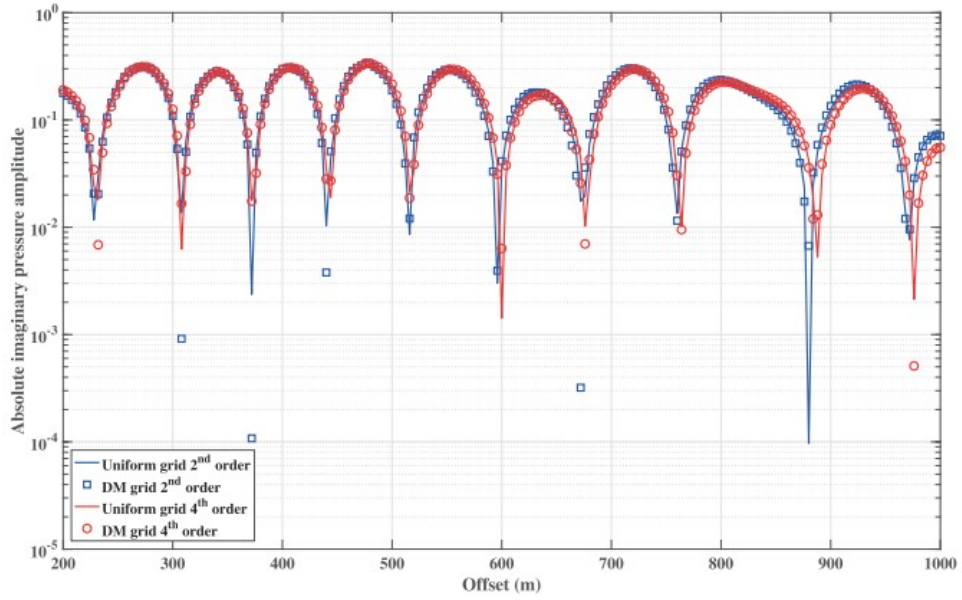

(b) Absolute imaginary part

Figure 8. Absolute real and imaginary parts of the pressure solution along the hill free surface for uniform and DM spatial discretizations using second- and fourth-order FD simulations.

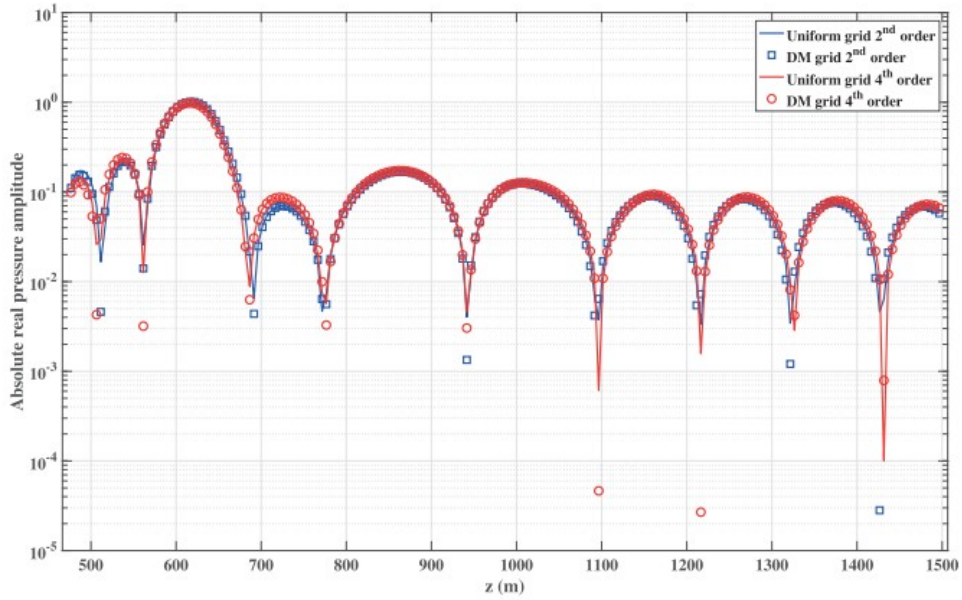

(a) Absolute real part

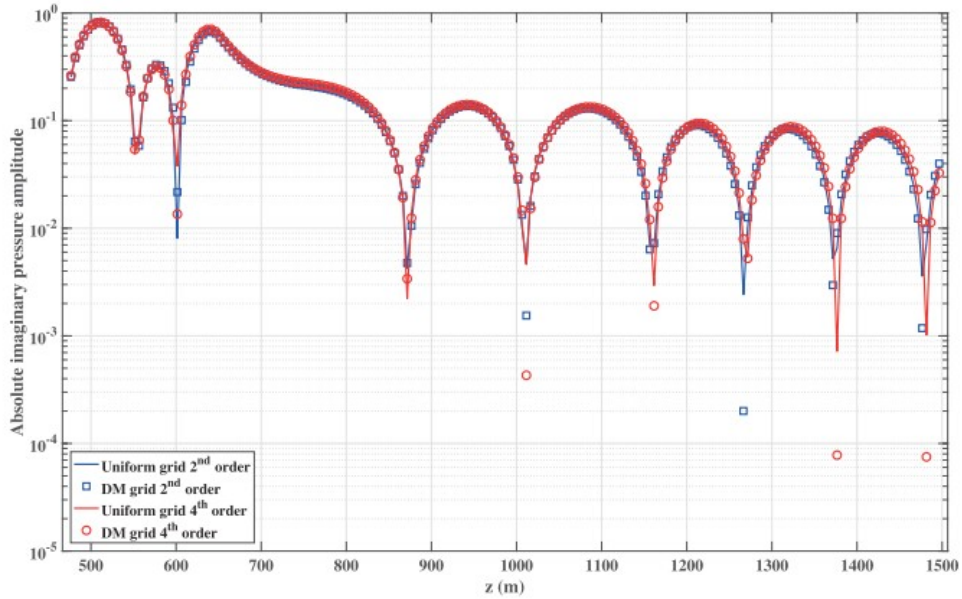

(b) Absolute imaginary part

Figure 9. Absolute real and imaginary parts of the pressure solution along the z direction of the hill surface model for uniform and DM spatial discretizations using second- and fourth-order FD simulations.

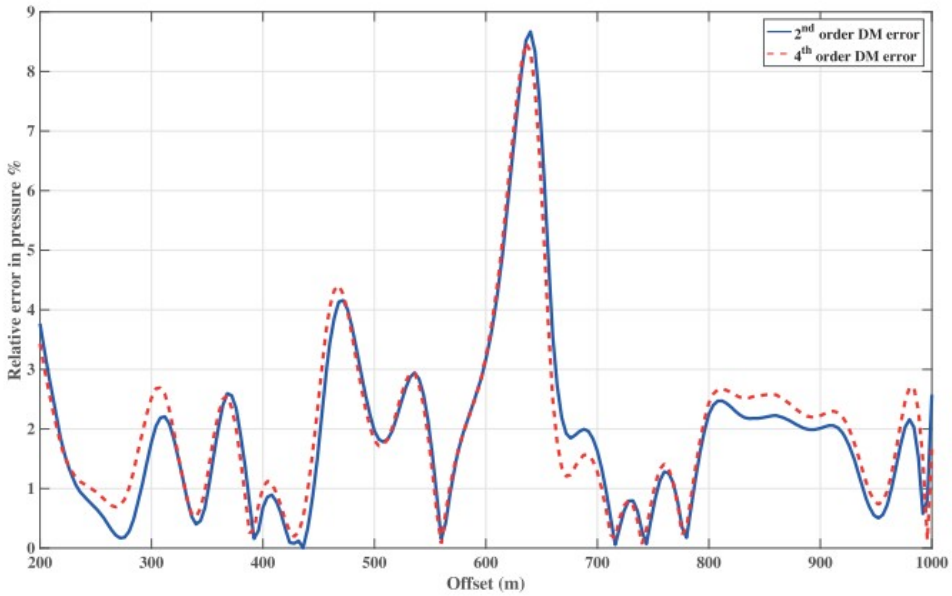

(a) Hill free surface line

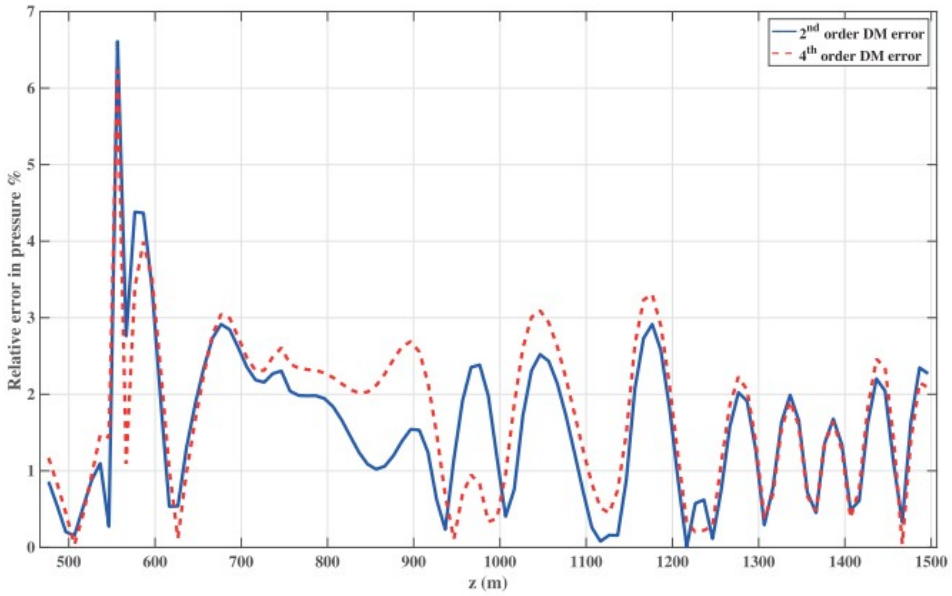

(b) z direction line

Figure 10. Absolute relative error in the pressure solution between uniform and DM spatial discretizations along the (a) free surface hill and (b) z direction using second- and fourth-order FD simulations. Here, the reference solution for the second-order DM FD is the second-order uniform fine mesh FD solution and the reference solution for fourth-order DM FD solution is the fourth-order uniform fine mesh FD solution.

3.3 Layered model with realistic topography

For our third accuracy test, we apply our DM scheme on a realistic topography surface provided by Saudi Aramco (see Fig. 11a). The provided model is large in size and contains a high-contrast layered velocity model. For the uniform simulations, we use a constant grid size of 10 m. We place

the DM interface at a depth of 720 m, above which the grid size is 10 m, and below which we use 15 m. The overlap zone contains two overlapping planes for the second-order DM FD simulations. We apply a Ricker wavelet point-source with a central frequency of 10 Hz that is located at (1000, 3000, 340) m (see Fig. 11b). Similar to our previous tests, both the uniform and DM FD simulations allow us to sample the minimum spatial wavelength by at least eight nodes. The frequency is reduced to 10 Hz to accommodate larger grid spacing for the spatially large realistic model.

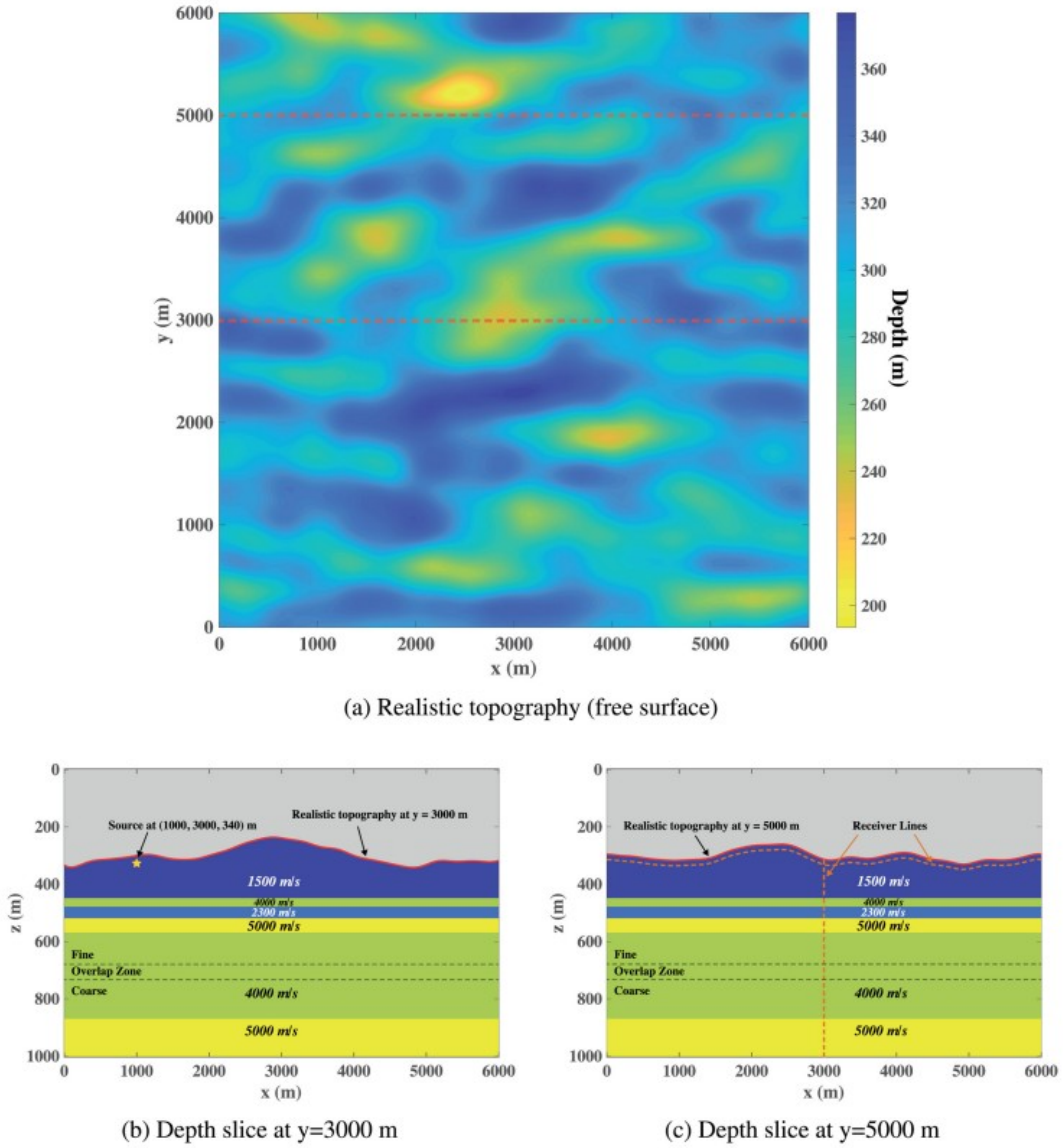

(a) Realistic topography (free surface)

(b) Depth slice at y=3000 m

(c) Depth slice at y=5000 m

Figure 11. (a) Realistic topography free surface with two *red* lines for cross-sections (b) at $y = 3000$ m and (c) at $y = 5000$ m. Cross-section (b) shows the source location and cross-section (c) shows the receiver lines.

We compare acoustic pressure solutions between the uniform and DM spatial discretizations at two receiver lines: one is aligned along and 10 m below the realistic free surface and the other is aligned along the z directions and located at $x = 3000$ m (see Fig. 11c). Similar to previous accuracy tests, the

solution from the DM is satisfactorily close to the uniform solution in both the real and imaginary parts (see Figs 12 and 13), with an average error of less than 5 per cent as shown in Fig. 14. In Fig. 14(a), some points show an inflated error that is caused by having a very small absolute acoustic pressure value near the free surface for the reference uniform fine mesh solution.

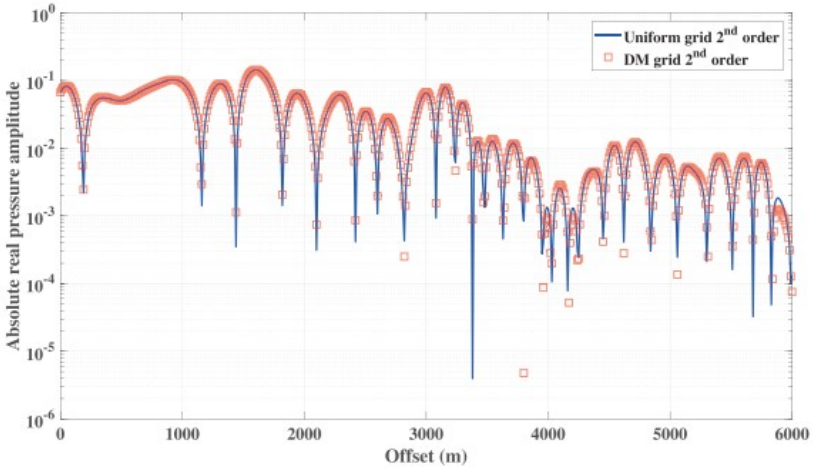

(a) Absolute real part

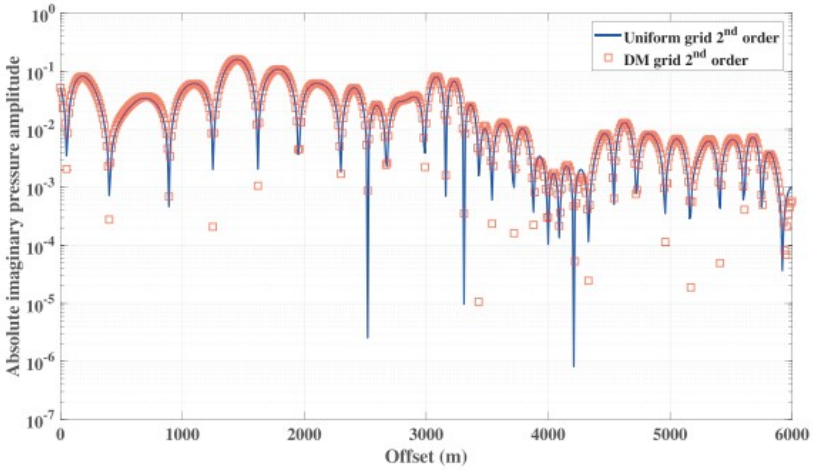

(b) Absolute imaginary part

Figure 12. Absolute real and imaginary parts of the pressure solution along the realistic topography free surface for uniform and DM spatial discretizations using second-order FD simulation.

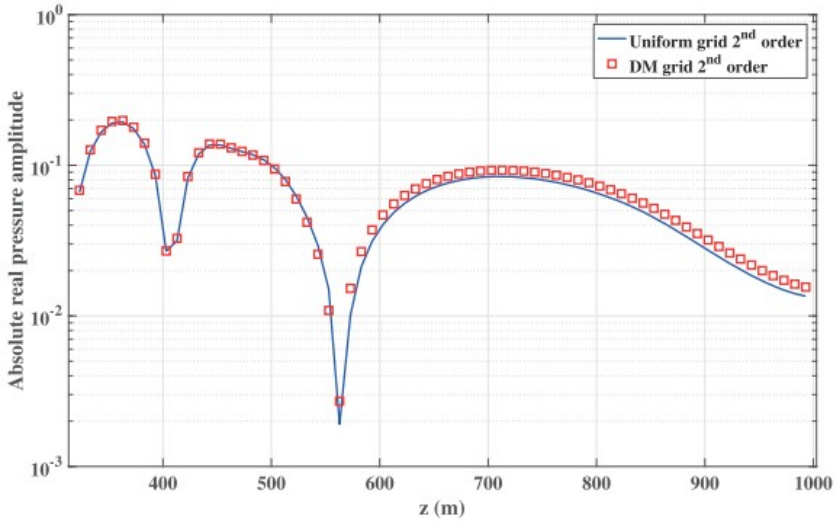

(a) Absolute real part

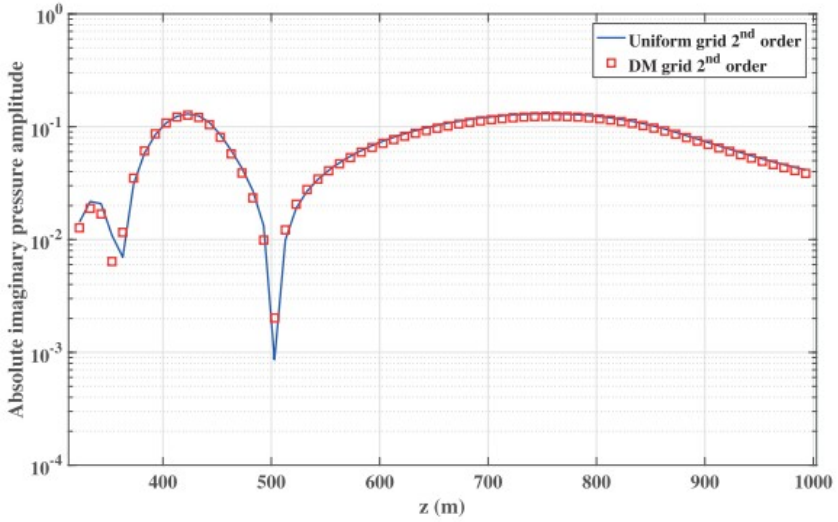

(b) Absolute imaginary part

Figure 13. Absolute real and imaginary parts of the pressure solution along the z direction of the realistic topography model for uniform and DM spatial discretizations using second-order FD simulation.

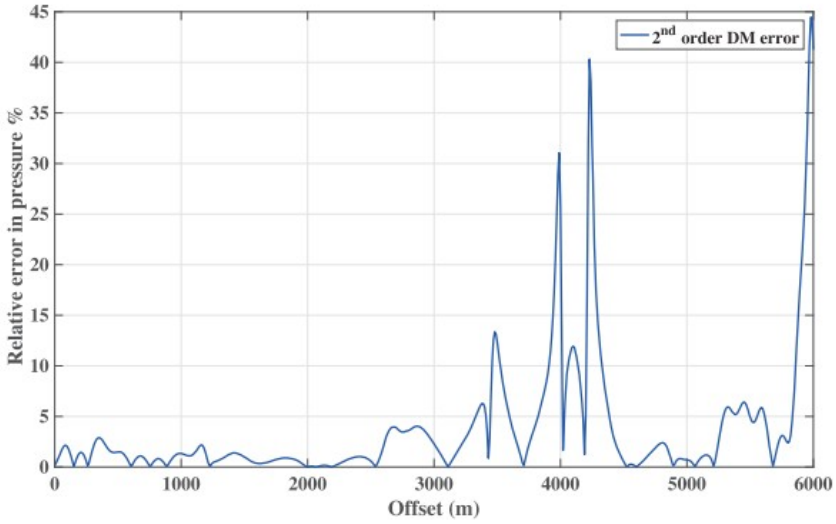

(a) Realistic topography line

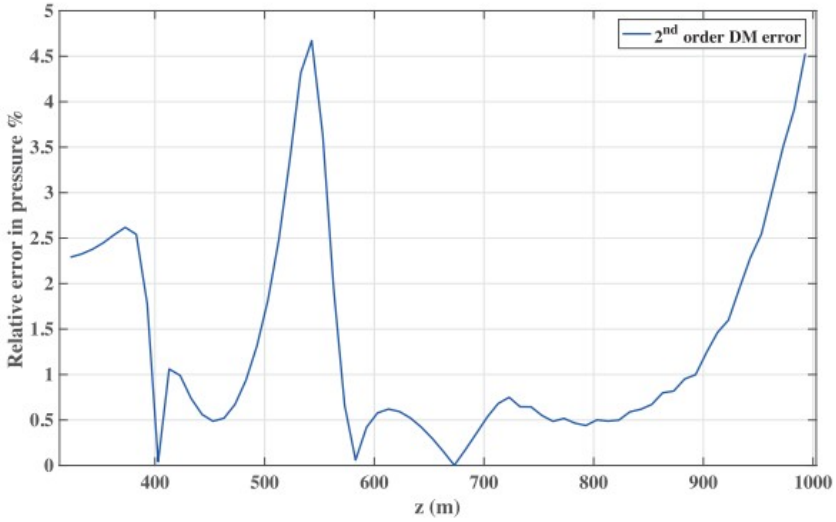

(b) z direction line

Figure 14. Absolute relative error in the pressure solution between uniform and DM spatial discretizations along the (a) realistic topography line and (b) z direction using second-order FD simulation. Here, the reference solution for the second-order DM FD is the second-order uniform fine mesh solution and the reference solution for fourth-order DM FD solution is the fourth-order uniform fine mesh FD solution.

Table 1. Second-order uniform mesh and DM FD benchmarks of the hill free surface model for several parallel direct and iterative solvers in PETSc numerical libraries.

Spatial discretization	Solver	Nodes	Cores per node	Matrix size	Iterations	Factor time (s)	Solve time (s)
Uniform	GMRES	64	32	13 450 500	17 713	0.00	28.01
DM	GMRES	64	32	8 228 000	16 222	0.00	15.88
DM	MUMPS	64	16	8 228 000	1	792.75	28.98
DM	MUMPS BLR	64	16	8 228 000	2	675.16	39.36
DM	SuperLU_DIST	64	16	8 228 000	1	278.03	5.05

4 EFFICIENCY AND CONVERGENCE ANALYSIS OF DM

As discussed above, computational efficiency and convergence is the justification for using a discontinuous staggered-grid mesh instead of a uniform mesh. In this section, we explore solution times for both spatial discretizations using direct and iterative solvers provided by PETSc numerical libraries (Balay *et al*. 2018). For the direct solvers, we tested MUMPS v5.1.2 (Amestoy *et al*. 2001, 2006), MUMPS Block Low Rank (BLR) with drop tolerance 10^{-7} (Amestoy *et al*. 2015) and SuperLU_DIST v5.1.3 (Li *et al*. 1999; Li & Demmel 2003; Grigori *et al*. 2007) and for the iterative solver, we tested the Generalized Minimal Residual (GMRES) method (Saad & Schultz 1986), all via PETSc. We use NERSC's Cray XC40 supercomputer (Cori), which has 2388 Intel Xeon 'Haswell' processor nodes. Each node has 128 GB DDR4 2133 MHz memory and holds two sockets where each socket is populated with a 16-core Intel® Xeon™ Processor E5–2698 v3 ('Haswell') at 2.3 GHz. We will test efficiency and convergence when implementing DM relative to uniform discretization for a layered velocity model with the hill free surface, and the spatiallylarge high-contrast layered velocity model with realistic topography.

4.1 Layered model with a hill as free surface

In the first test, we benchmark uniform and DM second- and fourth-order FD simulations of the layered hill free surface model (Fig. 7). To measure the speed gain without bias, we will use 64 nodes for all the simulations in this section and cap the number of cores per node to 16 for second-order FD and 8 for fourth-order FD to meet the direct solvers' high memory demands. The second-order FD scheme, which has approximately seven non-zeros per row in its matrix, shows a speed gain of 1.76 times for DM relative to the uniform fine mesh when using the GMRES iterative solver (Table 1 and Fig. 15a). The fourth-order FD scheme, which has approximately 19 non-zeros per row, shows a speed gain of 1.35 times (Table 2 and Fig. 15b).

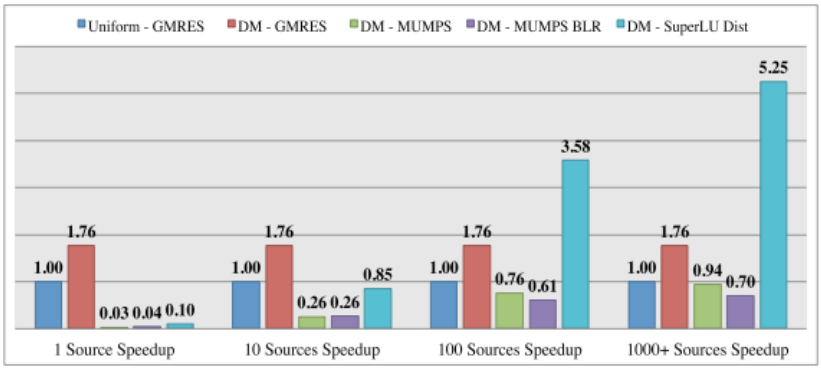

(a) Second-order

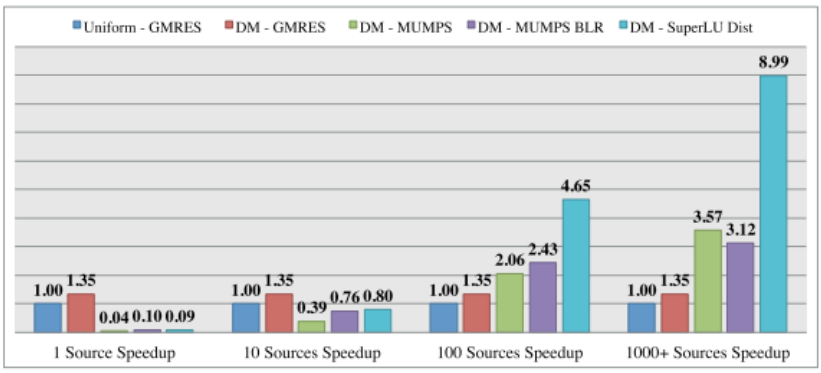

(b) Fourth-order

Figure 15. Speedup of (a) second- and (b) fourth-order uniform and DM FD solutions for different parallel direct and iterative solvers in PETSc numerical libraries.

Table 2. Fourth-order uniform mesh and DM FD benchmarks of the hill free surface model for several parallel direct and iterative solvers in PETSc numerical libraries.

Spatial discretization	Solver	Nodes	Cores per node	Matrix size	Iterations	Factor time (s)	Solve time (s)
Uniform	GMRES	64	32	13 450 500	23 022	0.00	117.44
DM	GMRES	64	32	8 228 000	20 908	0.00	86.96
DM	MUMPS	64	8	8 228 000	1	2 673.10	30.20
DM	MUMPS BLR	64	8	8 228 000	2	1 191.10	36.39
DM	SuperLU_DIST	64	8	8 228 000	1	1 352.30	11.71

Table 3. Second-order uniform and DM FD benchmarks of the realistic topography model for several parallel direct and iterative solvers in PETSc numerical libraries.

Spatial discretization	Solver	Nodes	Cores per node	Matrix size	Iterations	Factor time (s)	Solve time (s)
Uniform	GMRES	128	32	39 070 500		**The problem diverges**	
Uniform	MUMPS	128	4	39 070 500	1	3955.10	80.45
Uniform	MUMPS BLR	128	4	39 070 500	2	2229.00	106.97
Uniform	SuperLU_DIST	128	4	39 070 500		**Runs out of memory**	
DM	GMRES	128	32	31 010 012	20 940	0.00	105.76
DM	MUMPS	128	4	31 010 012	1	2658.60	58.40
DM	MUMPS BLR	128	4	31 010 012	2	1614.60	97.41
DM	SuperLU_DIST	128	4	31 010 012	1	1272.22	57.45

To measure the efficiency of direct solvers on DM simulations, we compare them against the GMRES iterative solver on uniform simulations for a large

number of sources, where each source is one right-hand side (RHS) in our acoustic wave equation formulation. For the second-order FD test, Fig. 15(a) shows a speed gain of more than five times when using SuperLU_DIST and a speed loss when using MUMPS for more than 1000 sources. The speed loss can be attributed to the favourable iterative conditions, which are the low number of non-zeros and small condition number due to the low velocity contrast between layers. The fourth-order simulation, which has a relatively higher number of non-zeros, shows a speed gain of nine times for SuperLU_DIST and more than three times for both MUMPS and MUMPS BLR when simulating for more than 1000 sources (Fig. 15b).

4.2 Layered model with realistic topography

To examine the influence of the large condition number and high number of non-zeros on solvers, we benchmark uniform mesh and DM second-order FD simulations of the high velocity contrast realistic topography model (Fig. 11). To keep the benchmarks fair, we use 128 nodes for all simulations and cap the number of cores per node to four for direct solvers.

Table 3 shows that the GMRES iterative solver diverges when using the uniform mesh and converges when using our DM discretization. Here, our DM lowers both the number of non-zeros and the condition number of the simulation matrix. We also observed that MUMPS is more memory efficient than SuperLU_DIST for large simulations (Table 3). In summary, our benchmarks indicate that DM discretization is faster and more stable than uniform discretization, especially for large models with high velocity contrasts.

5 CONCLUSION

We implemented a DM with embedded boundary for both second- and fourth-order accurate staggered-grid velocity-pressure FD schemes. It approximates the solution of the LF acoustic wave equation with any spacing ratio between the differently spaced regions. Our method applies trilinear interpolation to the coarse mesh to update pressure values at nodes needed by the fine mesh and it downsamples the fine mesh pressure values to update pressure values at nodes needed by the coarse mesh. We show that our DM with embedded boundary scheme is accurate when using two and six overlapping planes for second- and fourth-order FD approximation, respectively. For spatially large and high velocity contrast models, our DM scheme lowers the condition number and the problem size allowing iterative solvers to converge and direct solvers to require less memory. Our DM with embedded boundary FD scheme has the potential to significantly improve the efficiency of uniform FD methods, especially for simulations with realistic topographies, 3-D geological settings and near-surface low velocities. Therefore, the algorithm can become a powerful part of a forward-modelling engine used for full waveform inversion. It is also an important step towards realizing a DM solution for the elastic LF wave equation.

REFERENCES

AlSalem, H., Petrov, P., Newman, G. & Rector, J., 2018. Embedded boundary methods for modeling 3D finite-difference Laplace-Fourier domain acoustic-wave equation with free-surface topography, Geophysics, 83(5), T291–T300.

Amestoy, P., Ashcraft, C., Boiteau, O., Buttari, A., L'Excellent, J.-Y. & Weisbecker, C., 2015. Improving multifrontal methods by means of block low-rank representations, SIAM J. Sci. Comput., 37(3), A1451–A1474.

Amestoy, P.R., Duff, I.S., Koster, J. & L'Excellent, J.-Y., 2001. A fully asynchronous multifrontal solver using distributed dynamic scheduling, SIAM J. Matrix Anal. Appl., 23(1), 15–41.

Amestoy, P.R., Guermouche, A., L'Excellent, J.-Y. & Pralet, S., 2006. Hybrid scheduling for the parallel solution of linear systems, Parallel Comput., 32(2), 136–156.

Aoi, S. & Fujiwara, H., 1999. 3D finite-difference method using discontinuous grids, Bull. seism. Soc. Am., 89(4), 918–930.

Balay, S. et al., 2018. PETSc Web page. Available at: http://www.mcs.anl.gov/petsc, Accessed 31 March 2018.

Bao, H., Bielak, J., Ghattas, O., Kallivokas, L.F., O'Hallaron, D.R., Shewchuk, J.R. & Xu, J., 1998. Large-scale simulation of elastic wave propagation in heterogeneous media on parallel computers, Comput. Methods Appl. Mech. Eng., 152(1-2), 85–102.

Brewer, M.L. & Marcum, D. Casarotti, E., Stupazzini, M., Lee, S.J., Komatitsch, D., Piersanti, A. & Tromp, J., 2008. Cubit and seismic wave propagation based upon the spectral-element method: An advanced unstructured mesher for complex 3D geological media, in Proceedings of the 16th International Meshing Roundtable, pp. 579–597, Springer.

Fichtner, A., 2011. Full Seismic Waveform Modelling and Inversion, Springer.

Graves, R.W., 1996. Simulating seismic wave propagation in 3D elastic media using staggered-grid finite differences, Bull. seism. Soc. Am., 86(4), 1091–1106.

Grigori, L., Demmel, J.W. & Li, X.S., 2007. Parallel symbolic factorization for sparse LU with static pivoting, SIAM J. Sci. Comput., 29(3), 1289– 1314.

Hastings, F.D., Schneider, J.B. & Broschat, S.L., 1996. Application of the perfectly matched layer (pml) absorbing boundary condition to elastic wave propagation, J. acoust. Soc. Am., 100(5), 3061–3069.

Hayashi, K., Burns, D.R. & Toksoz, M.N., 2001. Discontinuous-grid finitedifference seismic modeling including surface topography, Bull. seism. Soc. Am., 91(6), 1750–1764.

Hustedt, B., Operto, S. & Virieux, J., 2004. Mixed-grid and staggered-grid finite-difference methods for frequency-domain acoustic wave modelling, Geophys. J. Int., 157(3), 1269–1296.

Jin, J.-M., 2015. The Finite Element Method in Electromagnetics,John Wiley & Sons.

Jo, C.-H., Shin, C. & Suh, J.H., 1996. An optimal 9-point, finite-difference, frequency-space, 2-D scalar wave extrapolator, Geophysics, 61(2), 529– 537.

Kim, S. & Pasciak, J.E., 2010. Analysis of a Cartesian pml approximation to acoustic scattering problems in r2, J. Math. Anal. Appl., 370(1), 168–186.

Komatitsch, D. & Tromp, J., 1999. Introduction to the spectral element method for three-dimensional seismic wave propagation, Geophys. J. Int., 139(3), 806–822.

Kristek, J., Moczo, P. & Galis, M., 2010. Stable discontinuous staggered grid in the finite-difference modelling of seismic motion, Geophys. J. Int., 183(3), 1401–1407.

Li, J., Zhang, Y. & Toksoz, M.N., 2010. Frequency-domain finite-difference ¨ acoustic modeling with free surface topography using embedded boundary method, in SEG Technical Program Expanded Abstracts 2010, pp. 2966–2971, Society of Exploration Geophysicists.

Li, X., Demmel, J., Gilbert, J., Grigori, I.L., Shao, M. & Yamazaki, I., 1999. SuperLU Users' Guide, Tech. Rep. LBNL-44289, Lawrence Berkeley National Laboratory.

Li, X.S. & Demmel, J.W., 2003. SuperLU DIST: A scalable distributedmemory sparse direct solver for unsymmetric linear systems, ACM Trans. Math. Softw., 29(2), 110–140.

Lysmer, J. & Drake, L.A., 1972. A finite element method for seismology, Methods Comput. Phys., 11, 181–216.

Marfurt, K.J., 1984. Accuracy of finite-difference and finite-element modeling of the scalar and elastic wave equations, Geophysics, 49(5), 533–549.

Moczo, P., 1989. Finite-difference technique for sh-waves in 2-D media using irregular grids–application to the seismic response problem, Geophys. J. Int., 99(2), 321–329.

Nie, S., Wang, Y., Olsen, K.B. & Day, S.M., 2017. Fourth-order staggeredgrid finite-difference seismic wavefield estimation using a discontinuous mesh interface (wedmi), Bull. seism. Soc. Am., 107(5), 2183–2193.

Operto, S., Virieux, J., Amestoy, P., L'Excellent, J.-Y., Giraud, L. & Ali, H.B.H., 2007. 3d finite-difference frequency-domain modeling of viscoacoustic wave propagation using a massively parallel direct solver: A feasibility study, Geophysics, 72(5), SM195–SM211.

Pasalic, D. & McGarry, R., 2010. A discontinuous mesh finite difference scheme for acoustic wave equations, in SEG Technical Program Expanded Abstracts 2010, pp. 2940–2944, Society of Exploration Geophysicists.

Petrov, P.V. & Newman, G.A., 2012. 3D finite-difference modeling of elastic wave propagation in the Laplace-Fourier domain, Geophysics, 77, T137–T155.

Pitarka, A., 1999. 3D elastic finite-difference modeling of seismic motion using staggered grids with nonuniform spacing, Bull. seism. Soc. Am., 89(1), 54–68.

Pratt, R.G. & Worthington, M., 1990. Inverse theory applied to multi-source cross-hole tomography. part 1: Acoustic wave-equation method, Geophys. Prospect., 38(3), 287–310.

Saad, Y. & Schultz, M.H., 1986. GMRES: A generalized minimal residual algorithm for solving nonsymmetric linear systems, SIAM J. Sci. Stat. Computing, 7(3), 856–869.

Stekl, I. & Pratt, R.G., 1998. Accurate viscoelastic modeling by frequency- ˇ domain finite differences using rotated operators, Geophysics, 63(5), 1779–1794.

Tessmer, E., 2000. Seismic finite-difference modeling with spatially varying time steps, Geophysics, 65(4), 1290–1293.

Virieux, J., 1986. P-sv wave propagation in heterogeneous media: Velocitystress finite-difference method, Geophysics, 51(4), 889–901.

Wang, Y., Xu, J. & Schuster, G., 2001. Viscoelastic wave simulation in basins by a variable-grid finite-difference method, Bull. seism. Soc. Am., 91(6), 1741–1749.

Zahradn´ık, J. & Urban, L., 1984. Effect of a simple mountain range on underground seismic motion, Geophys. J. Int., 79(1), 167–183.

Zhang, Y., 2017. Parallel Goal-Oriented Adaptive Finite Element Modeling For 3D Electromagnetic Exploration, Ph.D. thesis, San Diego State University.

Zhang, Z., Zhang, W., Li, H. & Chen, X., 2012. Stable discontinuous grid implementation for collocated-grid finite-difference seismic wave modelling, Geophys. J. Int., 192(3), 1179–1188.